

Elasticity of 2D ferroelectrics across their paraelectric phase transformation

Joseph E. Roll,¹ John M. Davis,¹ John W. Villanova,¹ and Salvador Barraza-Lopez^{1,2,*}

¹Department of Physics, University of Arkansas, Fayetteville, Arkansas 72701, United States

²MonArk NSF Quantum Foundry, University of Arkansas, Fayetteville, Arkansas 72701, United States

(Dated: March 16, 2022)

The mechanical behavior of two-dimensional (2D) materials across 2D phase changes is unknown, and the finite temperature (T) elasticity of paradigmatic SnSe monolayers—ferroelectric 2D materials turning paraelectric as their unit cell (u.c.) turns from a rectangle onto a square—is described here in a progressive manner. To begin with, their zero- T elastic energy landscape gives way to (Boltzmann-like) averages from which the elastic behavior is determined. These estimates are complemented with results from the strain-fluctuation method, which employs the energy landscape or *ab initio* molecular dynamics (MD) data. Both approaches capture the coalescence of elastic moduli $\langle C_{11}(T) \rangle = \langle C_{22}(T) \rangle$ due to the structural transformation. The broad evolution and sudden changes of elastic parameters $\langle C_{11}(T) \rangle$, $\langle C_{22}(T) \rangle$, and $\langle C_{12}(T) \rangle$ of these atomically-thin phase-change membranes establishes a heretofore overlooked connection among 2D materials and soft matter.

Introduction. Zero- T estimates of elastic parameters (sometimes called elastic *constants*) lose meaning on materials undergoing phase transitions (transformations) at finite T , where elastic behavior is expected to change drastically. For example, zero- T elastic parameters $C_{11}^{(0)}$ and $C_{22}^{(0)}$ have different magnitudes on materials with a rectangular (or orthorhombic in 3D) u.c., but these elastic moduli must turn identical at a critical T (T_c) in which the u.c. turns square (tetragonal, or cubic in 3D).

Group-IV monochalcogenide monolayers (MLs) are experimentally available [1–3] 2D ferroelectrics with a puckered *rectangular* u.c. and a Pnm2₁ group symmetry in their zero- T phase, whereby each atom is threefold coordinated [4–13]. They display *metavalent* bonding [14], characterized by large atomic effective charges, structural anharmonicity, and significant linear and non-linear optical responses. Their low- T crystal structure also underpins *anisotropic* elasticity [15, 16]. Nevertheless, these 2D materials undergo a firmly established structural change onto a fivefold coordinated *square* structure with P4/nmm symmetry at a critical temperature T_c ranging between 200 and 300 K [1–3, 10, 11, 13], at which their properties turn *isotropic*. Nothing has been said about the elastic behavior on their P4/nmm phase yet, and approaches based on (i) an analytical form of the zero- T elastic energy landscape [17], and (ii) the strain-fluctuation method [18] are deployed to answer this open question here.

Numerical methods. The elastic energy landscape and MD data were calculated with the *SIESTA* DFT code [19, 20] employing an exchange correlation functional with self-consistent van der Waals corrections [21]. Additional details can be found in Ref. [10].

Elasticity from elastic energy landscape. As illustrated on Fig. 1(a) for a SnSe ML (a paradigmatic group-IV monochalcogenide ML), a crystal elongated or compressed along two orthogonal directions a_1 and a_2 with a subsequent structural optimization of atomic positions for a given value of a_1 and a_2 leads to a zero- T elas-

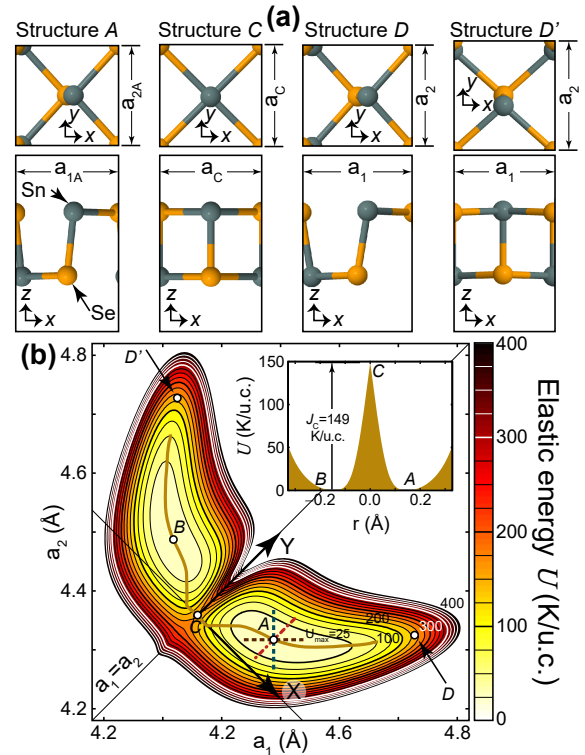


FIG. 1. (a) SnSe ML u.c. for points A, C, D, and D' on an analytical $U(a_1, a_2)$ [subplot (b)]. The solid curve connecting points A, C, and B on subplot (b) is the minimum-energy pathway among the two energy degenerate basins A and B, and the inset displays the energy barrier $J_C = U(ac, ac)$. Straight lines passing through point A were used to determine zero- T elastic moduli. Some isoenergy lines were drawn, too.

tic energy $E(a_1, a_2)$ per u.c. The change of energy $U(a_1, a_2) = E(a_1, a_2) - E(a_{1A}, a_{2A})$ with respect to a degenerate local minimum energy configuration—labeled A and having coordinates a_{1A} and a_{2A} —seen on Fig. 1(b) is an *elastic energy landscape* [22]. To simplify an eventual

extraction of partial derivatives, the landscape $U(a_1, a_2)$ in Fig. 1(b) is an analytical fit to raw *ab initio* data [10]. The raw data sets an energy barrier separating the two degenerate minima equal to $J_{C,r} = 149.25$ K/u.c., lattice parameters $a_{1A,r} = 4.4873$ Å, $a_{2A,r} = 4.3264$ Å at the energy minima A , and $a_C = 4.3590$ Å at for the square u.c. of lowest energy [10, 23].

$U(a_1, a_2)$ is mirror symmetric with respect to the $a_1 = a_2$ line on Fig. 1(b), thus calling for new variables:

$$X = (a_1 - a_2)/\sqrt{2}, \text{ and } Y = (a_1 + a_2 - 2a_C)/\sqrt{2}. \quad (1)$$

$X = 0$ and $Y = 0$ at point C (whose coordinates are $a_1 = a_2 = a_C$) which thus becomes the new origin of coordinates.

The mirror symmetry of the landscape about the $X = 0$ line makes $U(X, Y)$ even on X , and the following expression was used to fit numerical data [10]:

$$\begin{aligned} U(X, Y) = & J_C + \mathcal{U}_1 X^2 + \mathcal{U}_2 Y^2 + \mathcal{U}_3 Y X^2 \quad (2) \\ & + \mathcal{U}_4 Y^3 + \mathcal{U}_5 X^4 + \mathcal{U}_6 Y^4 \\ & + (\mathcal{U}_7 X e^{-\sqrt{X^2}/g_1} + \mathcal{U}_8 Y X e^{-\sqrt{X^2}/g_2}) \tanh(100X), \end{aligned}$$

with parameters and numerical uncertainties provided in Table I. With the exception of the terms on $\tanh(100X)$ —whose sole purpose is to smooth the cusp observed at the barrier in the numerical data [10]; see inset of Fig. 1(b)—the elastic energy landscape is a polynomial of order four. The quality of the fitting can be ascertained by noticing that its minima A is located at $(a_{1A}, a_{2A}) = (4.4896$ Å, 4.3173 Å) [or $X_A = 0.1218$ Å, $Y_A = 0.0629$ Å], which is less than 0.25% different from the raw *ab initio* data. One also notices that the saddle point on $U(X, Y)$ (i.e., the minimum energy barrier separating the two ground states A and B) occurs exactly at point a_C as determined in the raw data, and that $U(X_A, Y_A) = 0.0245$ K/u.c., leading to an energy barrier of 148.9755 K/u.c. which is only 0.2745 K/u.c. smaller than the one seen from the raw data.

Zero- T elastic moduli $C_{11}^{(0)}$, $C_{22}^{(0)}$ and $C_{12}^{(0)}$ are customarily obtained by fitting $U(a_1, a_2)$ to parabolas [15, 16]:

$$U \simeq \mathfrak{U} = \frac{1}{2} \epsilon^T \mathcal{C}^{(0)} \epsilon = \frac{C_{11}^{(0)} \epsilon_1^2}{2} + \frac{C_{22}^{(0)} \epsilon_2^2}{2} + C_{12}^{(0)} \epsilon_1 \epsilon_2, \quad (3)$$

where *strain* coordinates $\epsilon = (\epsilon_1, \epsilon_2)^T$ with

$$\epsilon_1 = (a_1 - a_{1A})/a_{1A}, \quad \epsilon_2 = (a_2 - a_{2A})/a_{2A}, \quad (4)$$

were employed. We recall that a_{1A} and a_{2A} in Eqn. (4) are zero- T equilibrium lattice parameters defining point A in the elastic energy landscape.

$\mathcal{C}^{(0)}$ is the *harmonic approximation* to the elasticity tensor, and \mathfrak{U} is the *harmonic approximation to U* . As acutely seen in Fig. 2(a), the prescription within Eqn. (3) neglects the strong anharmonicity of group-IV monochalcogenide MLs *by definition*. Further, given that

TABLE I. Fitting parameters for $U(X, Y)$. $J_C = 149$ K/u.c.

\mathcal{U}_1	$-3660.5 \pm 12.3\% \text{ K}/\text{Å}^2$	\mathcal{U}_2	$24849 \pm 4.3\% \text{ K}/\text{Å}^2$
\mathcal{U}_3	$-109410 \pm 8.2\% \text{ K}/\text{Å}^3$	\mathcal{U}_4	$-42945 \pm 21.2\% \text{ K}/\text{Å}^3$
\mathcal{U}_5	$188100 \pm 9.2\% \text{ K}/\text{Å}^4$	\mathcal{U}_6	$114840 \pm 43.4\% \text{ K}/\text{Å}^4$
\mathcal{U}_7	$-3568.5 \pm 13.4\% \text{ K}/\text{Å}$	\mathcal{U}_8	$-88140 \pm 12.4\% \text{ K}/\text{Å}^2$
g_1	$0.0583 \pm 9.3\% \text{ Å}$	g_2	$0.0536 \pm 8.1\% \text{ Å}$

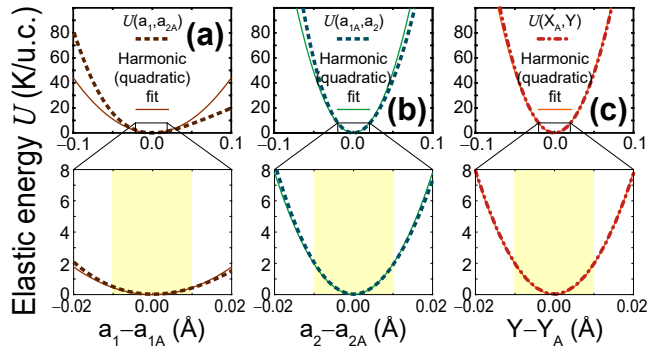


FIG. 2. Cuts of U along straight lines passing through point A on Fig. 1(b), and harmonic (i.e., quadratic) fits—thinner solid curves obtained within the shaded regions on the zoom-in plots—from which $C_{11}^{(0)}$, $C_{22}^{(0)}$, and $C_{12}^{(0)}$ were extracted.

elastic moduli are thermodynamical averages after all, *such approach misses a finite- T understanding of elasticity altogether*.

$U(X, Y)$ leads to zero- T elastic moduli consistent with prior work [15, 16]: Eqn. (2) is calculated along three straight lines [(a_1, a_{2A}), (a_{1A}, a_2), and (X_A, Y), corresponding to the brown (horizontal), green (vertical), and red (at 45°) straight lines passing through point A on Fig. 1(b), respectively] and Eqn. (3) is fitted against the parabolas displayed on Fig. 2. $C_{ij}^{(0)}$ are listed in Table II ($i, j = 1, 2$). Discrepancies with previous results (such as the smaller magnitude of $C_{11}^{(0)}$ and the slightly larger value of $C_{12}^{(0)}$ than $C_{11}^{(0)}$ here) are due to the use of different computational tools and exchange-correlation functionals in *ab initio* calculations. The softer $C_{11}^{(0)}$ here leads to a smaller T_c when contrasted to results using the numerical methods of Refs. [15, 16]; see Refs. [11] and [13] for a discussion.

To go beyond the zero- T paradigm, we make use of $U(X, Y)$ to determine elastic behavior next. A function of X and Y has an expectation value within the elastic energy landscape $\langle f(U_{max}) \rangle$ as an *average over classically accessible states* [17]:

$$\langle f(U_{max}) \rangle = \frac{\oint e^{-U(X,Y)/U_{max}} f(X, Y) dX dY}{\oint e^{-U(X,Y)/U_{max}} dX dY}, \quad (5)$$

with $dX dY$ an area element within the confines of a

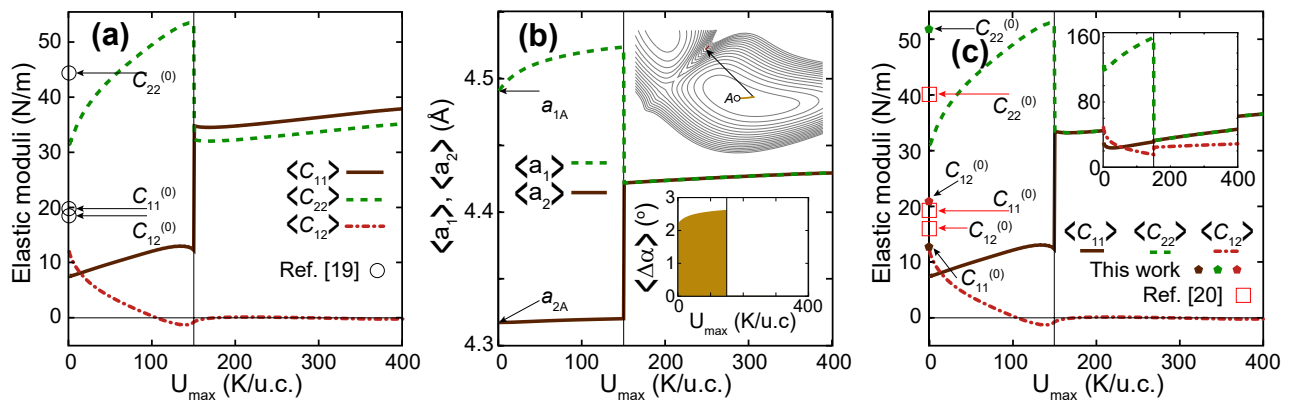


FIG. 3. (a) Elastic moduli as a function of U_{max} -isovalue, setting the strain with respect to a_{1A} and a_{2A} at zero- T . (b) Average lattice constants *versus* U_{max} : the u.c. turns from a rectangle ($\langle a_1 \rangle > \langle a_2 \rangle$) onto a square ($\langle a_1 \rangle = \langle a_2 \rangle$) when $U_{max} \geq J_C$. Insets: evolution of $\langle \Delta\alpha \rangle$ and of the point $(\langle a_1 \rangle, \langle a_2 \rangle)$ *versus* U_{max} . (c) Elastic moduli *versus* U_{max} , setting the strain with respect to $\langle a_1 \rangle$ and $\langle a_2 \rangle$ as obtained at subplot (b): $\langle C_{11} \rangle = \langle C_{22} \rangle$ are now identical past J_C . Inset: elastic moduli within the strain-fluctuation method. $C_{11}^{(0)}$, $C_{22}^{(0)}$, and $C_{12}^{(0)}$ as estimated by us and others are shown in subplots (a) and (c).

TABLE II. Zero- T in-plane elastic moduli (N/m).

Elastic modulus	Prior work	This work
$C_{11}^{(0)}$	19.9 [15], 19.2 [16]	12.7
$C_{22}^{(0)}$	44.5 [15], 40.1 [16]	51.8
$C_{12}^{(0)}$	18.6 [15], 16.0 [16]	20.9

isoenergy contour U_{max} around structure A , like those seen on Fig. 1(b).

Within this paradigm, $U(X, Y)$ is a classical potential energy profile, and a set of accessible *crystalline configurations* lies within isoenergy confines. [U_{max} is the largest kinetic energy of a hypothetical particle in the landscape, and is thus indirectly linked to T that way.] For example, sampled u.c.s will all have $a_1 > a_2$ when the U_{max} isoenergy curve is smaller than J_C . This is, the sampled structures will all be *ferroelectric*, having an in-plane polarization along the x -direction [10]; see structure A on Fig. 1(a). When $U_{max} \geq J_C$ nevertheless, the *average structure* encompasses minima A and B yielding $a_1 = a_2$, and it thus is a square. The fact that $a_1 = a_2$ on average when $U_{max} \geq J_C$ is illustrated by structures D and D' on Fig. 1(b), which have x - and y -coordinates swapped. In this sense, the averaging among *crystalline configurations* within the energy landscape up to an energy U_{max} achieves an effect similar to T : a transformation whereby the average u.c. turns from a rectangle onto a square. A caveat to this model is that it is based on *averaging over independent crystalline* u.c.s, while 2D structural transformations in 2D are driven by disorder [8, 9].

Energy average values for C_{ij} are determined by [17]:

$$\langle C_{ij}(U_{max}) \rangle = k_B \left\{ \left\langle \frac{\partial^2 u}{\partial \epsilon_i \partial \epsilon_j} \right\rangle - \frac{1}{U_{max}} \left[\left\langle \mathcal{A} \frac{\partial u}{\partial \epsilon_i} \frac{\partial u}{\partial \epsilon_j} \right\rangle - \langle \mathcal{A} \right] \left\langle \frac{\partial u}{\partial \epsilon_i} \right\rangle \left\langle \frac{\partial u}{\partial \epsilon_j} \right\rangle \right\}, \quad (6)$$

with k_B Boltzmann's constant, $\mathcal{A} = a_1 a_2$, and $u = U/\mathcal{A}$.

Eqn. (6) was evaluated numerically for energy isovalues U_{max} starting at 1K/u.c and up to 400 K/u.c. [Fig. 3(a)]. Near $U_{max} = 0$, the averaging procedure yields elastic moduli smaller than those listed in Table II. Within this method, $\langle C_{12} \rangle$ quickly decays to a nearly zero value and it becomes negative (for an auxetic behavior). On the other hand, $\langle C_{22} \rangle > \langle C_{11} \rangle$ by a factor in between 3 and 5 for energies up to $U_{max} = J_C$, at which a sharp change occurs whereby $\langle C_{22} \rangle \approx \langle C_{11} \rangle$.

The fact that $\langle C_{22} \rangle \neq \langle C_{11} \rangle$ for isovalues $U_{max} \geq J_C$, in which the average structure already turned isotropic [see Fig. 3(b)], represents an inaccuracy of the approach in Ref. [17]. It originates from the fact that strain was written out with respect to the zero- T ground state structure (a_{1A}, a_{2A}) in Eqn. (4). Experimentally, strain at finite- T is measured with respect to a structure in *thermal equilibrium*, calling for a calculation of elastic moduli in which average values of a_1 and a_2 are employed. Strain is then redefined as:

$$\epsilon_1 = \frac{a_1 - \langle a_1 \rangle}{\langle a_1 \rangle}, \quad \text{and} \quad \epsilon_2 = \frac{a_2 - \langle a_2 \rangle}{\langle a_2 \rangle}, \quad (7)$$

which is still valid at zero- T in which $\langle a_i \rangle = a_{iA}$ ($i = 1, 2$) The resulting elastic parameters are shown in Fig. 3(c). Now, $\langle C_{22} \rangle = \langle C_{11} \rangle$ for isovalues $U_{max} \geq J_C$. The use of Eqn. (7) instead of Eqn. (4) is thus a correction to our previous method [17].

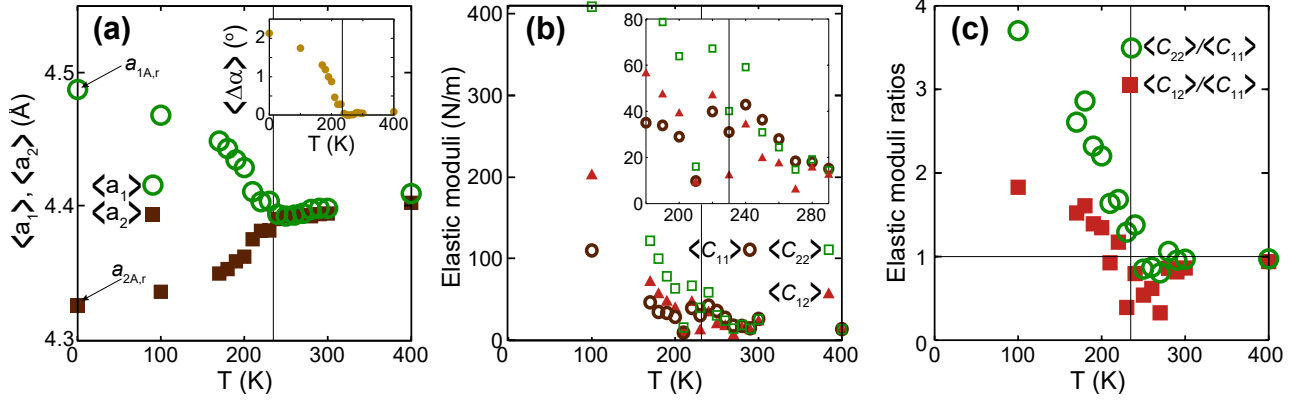


FIG. 4. (a) $\langle a_1 \rangle$ and $\langle a_2 \rangle$ versus T on MD calculations. Inset: $\langle \Delta\alpha \rangle$. (b) Elastic moduli from the strain-fluctuation method and $\langle \epsilon_i \epsilon_j \rangle$, $\langle \epsilon_i \rangle$ ($i = 1, 2$) determined from MD: see the coalescence of $\langle C_{11} \rangle$ and $\langle C_{22} \rangle$ past T_C , and the similar magnitudes of $\langle C_{ij} \rangle$ to those seen at the inset of Fig. 3(c). (c) Ratio among the elastic moduli displayed in subplot (b).

$\langle C_{12} \rangle$ is the softest elastic modulus on this model. On the other hand, $\langle C_{11} \rangle$ hardens significantly at the transition ($U_{max} = J_C$), while $\langle C_{22} \rangle$ suddenly softens at $U_{max} = J_C$. According to Fig. 3, a SnSe ML is much softer than graphene, for which $C_{11}^{(0)} = C_{22}^{(0)} = 336$ N/m, and $C_{12}^{(0)} = 75$ N/m (see Ref. [24], and multiply by half of Bernal graphite’s unit cell thickness $\simeq 3.4$ Å).

We propose—by direct comparison among J_C and T_C from numerical calculations [11]—a linear correspondence among these two variables ($T \propto 1.42U_{max}$) for this material, such that $T_C = 212$ K, and finite- T elastic behavior can be extracted from Fig. 3 at a low computational cost.

Elasticity from the strain-fluctuation method. We next employ the strain-fluctuation method to determine the elastic moduli. The expression to work with is [18]:

$$\langle C^{-1}_{ij} \rangle = \frac{\langle \mathcal{A} \rangle}{k_B T} (\langle \epsilon_i \epsilon_j \rangle - \langle \epsilon_i \rangle \langle \epsilon_j \rangle), \quad (8)$$

which is less convoluted than Eqn. (6), and also amenable for MD input.

Computed using $U(X, Y)$, $\langle \epsilon_i \rangle = \frac{\langle a_i \rangle - \langle a_i \rangle}{\langle a_i \rangle} = \frac{\langle a_i \rangle - \langle a_i \rangle}{\langle a_i \rangle} = 0$ ($i = 1, 2$) for additional simplification, and $\langle C_{ij} \rangle$ ($i, j = 1, 2$) are displayed as an inset on Fig. 3(c). One notes that $\langle C_{ij} \rangle > 0$ now, so that auxetic behavior cannot be confirmed within the strain-fluctuation method. A second point to notice is that $\langle C_{22} \rangle$ now becomes three times larger than its biggest magnitude obtained using Eqn. 6. For $U_{max} < J_C$, $\langle C_{11} \rangle$ is about twice as large than its magnitude from Eqn. 6, too. $\langle C_{11} \rangle = \langle C_{22} \rangle$ for $U_{max} \geq J_C$, with a magnitude now comparable to that obtained from Eqn. 6. The two takeouts from the strain-fluctuation approach [inset on Fig. 3(c)] are that $\langle C_{22} \rangle$ is much larger than its estimate using partial derivatives of $U(X, Y)$, and that $\langle C_{21} \rangle$ remains larger than zero.

The Pnm2₁ to P4/nmm structural transformation is signaled by a collapse of the rhombic distortion angle $\langle \Delta\alpha \rangle$ [related to a_1 and a_2 as $\langle \Delta\alpha \rangle = \left(\frac{\langle a_1 \rangle}{\langle a_2 \rangle} - 1 \right) \frac{180^\circ}{\pi}$] to a zero value [1, 10]. As seen at an inset on Fig. 3(b), $U(X, Y)$ does yield the required collapse of $\langle \Delta\alpha \rangle$, but it does not display a gradual decrease with a critical exponent of 1/3 [1, 10] as the inset on Fig. 4(a)—obtained from MD—does. This is so because $U(X, Y)$ makes $\langle a_1 \rangle$ plow to larger values while $\langle a_2 \rangle$ remains relatively unchanged up to $U_{max} = J_C$, when both lattice parameters change *discontinuously* onto an identical value [see Fig. 3(b) and its upper inset].

And thus, while an estimation of elastic properties based on $U(X, Y)$ [using either Eqn. (6), or Eqn. (8)] is relatively inexpensive, MD data was also utilized to estimate $\langle C_{11} \rangle$, $\langle C_{22} \rangle$, and $\langle C_{12} \rangle$ within the strain-fluctuation approach. Briefly, 16×16 supercells containing 1024 atoms were employed on NPT *ab initio* MD calculations for sixteen different T s in between 100 and 400 K. 20,000 individual timesteps with a 1.5 fs resolution were obtained for any given T . Thermal averages were obtained for times above 5 ps to allow for proper thermalization. In this approach, $\epsilon_i = \frac{1}{2} [(\langle h \rangle^{-1T} h^T h \langle h \rangle^{-1})_{ii} - 1]$ ($i = 1, 2$) [18]. $h = (\mathbf{a}_1, \mathbf{a}_2)$, and $\langle h \rangle = (\langle \mathbf{a}_1 \rangle, \langle \mathbf{a}_2 \rangle)$ are 2×2 matrices containing the in-plane magnitudes of supercell lattice vectors \mathbf{a}_1 and \mathbf{a}_2 , which are written in column form. The matrix h contains the in-plane superlattice constants for one MD step, and $\langle h \rangle$ is its average over the available MD steps past thermalization. Here, $\langle \mathcal{A} \rangle$ is replaced by the supercell’s area thermal average.

The results, shown in Figs. 4(b) and 4(c), indicate a magnitude of $\langle C_{22} \rangle$ comparable with that of graphene at 100 K [24], but a softer magnitude of $\langle C_{11} \rangle$ that is four times smaller, as it is expected due to the SnSe ML’s anisotropy. All elastic constants then decrease, in a manner similar to that seen at the inset of Fig. 3(c). $\langle C_{ii} \rangle$

($i = 1, 2$) turn similar despite of method employed at energies/temperatures above the transition.

Conclusion. The finite- T elastic behavior of a paradigmatic 2D ferroelectric was estimated from second-order partial derivatives of the energy on their zero- T elastic energy landscape, and following the prescriptions of the strain-fluctuation method as well. Within the later method, average strain was introduced utilizing either the elastic energy landscape, or dedicated *ab initio* MD data. Despite of method, $\langle C_{11} \rangle$ are shown to coalesce past the transition energy J_C or temperature T_C , and the elastic moduli turns much softer than that determined on graphene. The results contained here thus show how to understand the finite- T elastic behavior of 2D materials undergoing two-dimensional transformations.

The authors acknowledge Dr. P. Kumar for insightful conversations, as well as support from the U.S. Department of Energy (J.W.V. was funded by Award DE-SC0016139, and S.B.L. by Award DE-SC0022120).

* sbarraza@uark.edu

- [1] K. Chang, J. Liu, H. Lin, N. Wang, K. Zhao, A. Zhang, F. Jin, Y. Zhong, X. Hu, W. Duan, et al., *Science* **353**, 274 (2016).
- [2] K. Chang, F. Küster, B. J. Miller, J.-R. Ji, J.-L. Zhang, P. Sessi, S. Barraza-Lopez, and S. S. P. Parkin, *Nano Lett.* **20**, 6590 (2020).
- [3] N. Higashitarumizu, H. Kawamoto, C.-J. Lee, B.-H. Lin, F.-H. Chu, I. Yonemori, T. Nishimura, K. Wakabayashi, W.-H. Chang, and K. Nagashio, *Nat. Commun.* **11**, 2428 (2020).
- [4] Y. Ye, Q. Guo, X. Liu, C. Liu, J. Wang, Y. Liu, and J. Qiu, *Chem. Mater.* **29**, 8361 (2017).
- [5] C. Cui, F. Xue, W.-J. Hu, and L.-J. Li, *npj 2D Mater. Appl.* **2**, 18 (2018).
- [6] M. Wu and P. Jena, *Wiley Interdiscip. Rev. Comput. Mol. Sci.* **8**, e1365 (2018).
- [7] Z. Guan, H. Hu, X. Shen, P. Xiang, N. Zhong, J. Chu, and C. Duan, *Adv. Electron. Mater.* **6**, 1900818 (2020).
- [8] M. Mehboudi, A. M. Dorio, W. Zhu, A. van der Zande, H. O. H. Churchill, A. A. Pacheco-Sanjuan, E. O. Harriss, P. Kumar, and S. Barraza-Lopez, *Nano Lett.* **16**, 1704 (2016).
- [9] M. Mehboudi, B. M. Fregoso, Y. Yang, W. Zhu, A. van der Zande, J. Ferrer, L. Bellaiche, P. Kumar, and S. Barraza-Lopez, *Phys. Rev. Lett.* **117**, 246802 (2016).
- [10] S. Barraza-Lopez, T. P. Kaloni, S. P. Poudel, and P. Kumar, *Phys. Rev. B* **97**, 024110 (2018).
- [11] J. W. Villanova, P. Kumar, and S. Barraza-Lopez, *Phys. Rev. B* **101**, 184101 (2020).
- [12] J. W. Villanova and S. Barraza-Lopez, *Phys. Rev. B* **103**, 035421 (2021).
- [13] S. Barraza-Lopez, B. M. Fregoso, J. W. Villanova, S. S. P. Parkin, and K. Chang, *Rev. Mod. Phys.* **93**, 011001 (2021).
- [14] I. Ronneberger, Z. Zanolli, M. Wuttig, and R. Mazzarello, *Adv. Mater.* **32**, 2001033 (2020).
- [15] R. Fei, W. Li, J. Li, and L. Yang, *Appl. Phys. Lett.* **107**, 173104 (2015).
- [16] L. C. Gomes, A. Carvalho, and A. H. Castro Neto, *Phys. Rev. B* **92**, 214103 (2015).
- [17] A. Pacheco-Sanjuan, T. B. Bishop, E. E. Farmer, P. Kumar, and S. Barraza-Lopez, *Phys. Rev. B* **99**, 104108 (2019).
- [18] J. R. Ray, *Comp. Phys. Rep.* **8**, 109 (1988).
- [19] R. M. Martin, *Electronic Structure: Basic Theory and Practical Methods* (Cambridge U. Press, 2004).
- [20] J. M. Soler, E. Artacho, J. D. Gale, A. García, J. Junquera, P. Ordejón, and D. Sánchez-Portal, *J. Phys.: Condens. Matter* **14**, 2745 (2002).
- [21] G. Román-Pérez and J. M. Soler, *Phys. Rev. Lett.* **103**, 096102 (2009).
- [22] D. J. Wales, *Energy Landscapes: Applications to Clusters, Biomolecules and Glasses* (Cambridge U. Press, Cambridge, UK, 2003).
- [23] S. P. Poudel, J. W. Villanova, and S. Barraza-Lopez, *Phys. Rev. Materials* **3**, 124004 (2019).
- [24] S. Thomas, K. Ajith, S. U. Lee, and M. C. Valsakumar, *RSC Adv.* **8**, 27283 (2018).